

# Noninvasive Imaging of Cycling Hypoxia in Head and Neck Cancer Using Intrinsic Susceptibility MRI



Rafal Panek<sup>1,2,3</sup>, Liam Welsh<sup>2,3</sup>, Lauren C.J. Baker<sup>1,2</sup>, Maria A. Schmidt<sup>1,2,3</sup>, Kee H. Wong<sup>2,3</sup>, Angela M. Riddell<sup>1,2,3</sup>, Dow-Mu Koh<sup>1,2,3</sup>, Alex Dunlop<sup>2,3</sup>, Dualta McQuaid<sup>2,3</sup>, James A. d'Arcy<sup>1,2,3</sup>, Shreerang A. Bhide<sup>2,3</sup>, Kevin J. Harrington<sup>2,3</sup>, Christopher M. Nutting<sup>3</sup>, Georgina Hopkinson<sup>3</sup>, Cheryl Richardson<sup>3</sup>, Carol Box<sup>2</sup>, Suzanne A. Eccles<sup>2</sup>, Martin O. Leach<sup>1,2,3</sup>, Simon P. Robinson<sup>1,2</sup>, and Kate L. Newbold<sup>2,3</sup>

## Abstract

**Purpose:** To evaluate intrinsic susceptibility (IS) MRI for the identification of cycling hypoxia, and the assessment of its extent and spatial distribution, in head and neck squamous cell carcinoma (HNSCC) xenografts and patients.

**Experimental Design:** Quantitation of the transverse relaxation rate,  $R_2^*$ , which is sensitive to paramagnetic deoxyhemoglobin, using serial IS-MRI acquisitions, was used to monitor temporal oscillations in levels of paramagnetic deoxyhemoglobin in human CAL<sup>R</sup> xenografts and patients with HNSCC at 3T. Autocovariance and power spectrum analysis of variations in  $R_2^*$  was performed for each imaged voxel, to assess statistical significance and frequencies of cycling changes in tumor blood oxygenation. Pathologic correlates with tumor perfusion (Hoechst 33342), hypoxia (pimonidazole), and vascular density (CD31) were sought in the xenografts, and dynamic contrast-enhanced (DCE)

MRI was used to assess patient tumor vascularization. The prevalence of fluctuations within patient tumors, DCE parameters, and treatment outcome were reported.

**Results:** Spontaneous  $R_2^*$  fluctuations with a median periodicity of 15 minutes were detected in both xenografts and patient tumors. Spatially, these fluctuations were predominantly associated with regions of heterogeneous perfusion and hypoxia in the CAL<sup>R</sup> xenografts. In patients,  $R_2^*$  fluctuations spatially correlated with regions of lymph nodes with low  $K^{trans}$  values, typically in the vicinity of necrotic cores.

**Conclusions:** IS-MRI can be used to monitor variations in levels of paramagnetic deoxyhemoglobin, associated with cycling hypoxia. The presence of such fluctuations may be linked with impaired tumor vasculature, the presence of which may impact treatment outcome. *Clin Cancer Res*; 23(15); 4233–41. ©2017 AACR.

## Introduction

Understanding the tumor microenvironment is essential for the delivery of personalized cancer treatment (1–3). Hypoxia, resulting from an imbalance between oxygen delivery and consumption, is an important component of the tumor microenvironment that influences the response to both radiotherapy and chemotherapy (2, 4, 5). Tumor hypoxia is a well-established cause of treatment resistance, and adversely affects the prognosis of head and neck squamous cell carcinoma (HNSCC; ref. 6). Furthermore,

targeting tumor hypoxia has been validated as a therapeutic strategy in HNSCC (6, 7), and its modification during standard radiotherapy can improve outcomes in terms of locoregional control, disease-specific survival, and overall survival (8).

Historically, the low oxygen tension associated with tumors was considered to be a consequence of chronic or diffusion-limited hypoxia (9), and acute or perfusion-limited hypoxia (10). It is now clear that this is an oversimplification and that the tumor microenvironment is highly dynamic and contains subpopulations of cancer cells exposed to continuously changing gradients of oxygen, nutrients, and pH (11). These microenvironmental components can promote genomic instability within cancer cells, providing an overall selective advantage for malignant growth (12). For example, tumors may contain cells that have been differentially exposed to hypoxia for minutes to hours and then reoxygenated (13–15). This process can recur, leading to "cycling" hypoxia (16–18). Cycling hypoxia arises from variations in red blood cell (RBC) flux through the abnormal tumor vasculature (16, 18, 19). Several factors may contribute to such fluctuations, including arteriolar vasomotion (20, 21), rapid vascular modeling (22), disorganized vascular hierarchy (23, 24), or increased transcapillary permeability (25).

Experimental evidence suggests that hypoxia and anoxia can alter tumor cell-cycle checkpoint control and the sensing and

<sup>1</sup>CR-UK and EPSRC Cancer Imaging Centre, London, United Kingdom. <sup>2</sup>Institute of Cancer Research, London, United Kingdom. <sup>3</sup>Royal Marsden Hospital, London, United Kingdom.

**Note:** Supplementary data for this article are available at Clinical Cancer Research Online (<http://clincancerres.aacrjournals.org/>).

S.P. Robinson and K.L. Newbold share senior authorship.

S.P. Robinson led on preclinical and K.L. Newbold on clinical aspects of the work.

**Corresponding Author:** Martin O. Leach, The Institute of Cancer Research, Cotswold Road, Sutton, Surrey SM2 5NG, United Kingdom. Phone: 44-20-8661-3338; Fax: 44-20-8661-0846; E-mail: martin.leach@icr.ac.uk

doi: 10.1158/1078-0432.CCR-16-1209

©2017 American Association for Cancer Research.

### Translational Relevance

The presence of cycling hypoxia is a key determinant of radioresistance, impaired drug delivery, and increased metastatic potential in head and neck squamous cell carcinoma (HNSCC). Noninvasive imaging strategies to identify and assess the magnitude and distribution of acutely hypoxic tumor cell subpopulations *in situ* may provide prognostic and predictive biomarkers for the treatment of HNSCC. Quantitation of the transverse relaxation rate,  $R_2^*$ , using intrinsic susceptibility MRI can be used to serially monitor variations in levels of paramagnetic deoxyhemoglobin, associated with cycling hypoxia, both in HNSCC xenografts and patients on a clinical 3T system. Such fluctuations are predominantly associated with regions of impaired tumor vasculature, the presence of which may be linked to a poorer outcome.

repair of DNA damage (12, 26, 27). Preclinical studies have shown that the homologous recombination DNA repair pathway is suppressed by chronic hypoxia, whereas DNA damage-associated checkpoint cell-cycle arrest and nonhomologous end joining are stimulated by acute hypoxia (12, 27). These factors lead to radioresistance, decreased delivery of cytotoxics, and increased metastatic potential. Therefore, detecting the magnitude and distribution of acutely and chronically hypoxic tumor cell subpopulations may determine their prognostic and predictive value in HNSCC and help in the selection of optimal therapeutic strategies (2).

Advances in imaging techniques can now provide a means of defining noninvasive quantitative biomarkers to inform on biologically relevant structure–function relationships in tumors, enabling their accurate detection, an understanding of their behavior, and report on response to treatment. One such approach, intrinsic susceptibility MRI (IS-MRI), involves quantitation of the transverse relaxation rate  $R_2^*$ , which is sensitive to the concentration of paramagnetic deoxyhemoglobin within the vascular compartment of tissues. Compared with most normal tissues, tumors typically exhibit relatively fast  $R_2^*$  values, a consequence of the high concentration of deoxygenated RBCs within the typically chaotic and unstable microcirculation. However, the strength of the correlation between tissue  $R_2^*$  and oxygen partial pressure, measured *in situ* using oxygen probes, or via IHC detection of reduced 2-nitroimidazole adducts, has been reported to be at best moderate (28). This is likely due to the dependence of  $R_2^*$  on a number of physiologic factors, including blood volume, hematocrit, and vessel caliber (28–30). However, variations in these parameters can be greatly compensated for, and data interpretation simplified, through assessing modulation of  $R_2^*$  with, for example, hyperoxic gas challenge, or injection of vascular contrast agents. It is also possible to temporally monitor changes in  $R_2^*$  using continuous IS-MRI measurements, which have been exploited preclinically to noninvasively image cycling hypoxia at high spatial and temporal resolution in tumors propagated in mice (31–33).

In this study, IS-MRI was initially used to measure spontaneous  $R_2^*$  fluctuations in mice bearing HNSCC xenografts on a clinical 3T MRI scanner, and pathologic correlates sought.

Subsequently, the preclinical IS-MRI methodology was translated to a clinical pilot study of patients with locally advanced HNSCC, also imaged at 3T.

## Materials and Methods

### Preclinical imaging

Experiments were performed in compliance with Home Office licenses issued under the UK Animals (Scientific Procedures) Act 1986 following local ethical approval, the United Kingdom National Cancer Research Institute guidelines for animal welfare in cancer research (34) and with the ARRIVE guidelines (35). Adult female athymic NCr nu/nu mice ( $n = 5$ , 7–8 weeks old, Charles River Laboratories) were injected subcutaneously in the flank with  $5 \times 10^5$  human CAL<sup>R</sup> HNSCC cells, stably resistant to EGFR tyrosine kinase inhibitors. The CAL<sup>R</sup> xenograft doubling time *in vivo* is approximately 4 days (36). Tumor volume was monitored using calipers and the formula for an ellipsoid,  $(\pi/6) \times L \times W \times D$ , where  $L$ ,  $W$ , and  $D$  are the largest orthogonal dimensions of the ellipsoid. Tumors were imaged at volumes of approximately 500 mm<sup>3</sup>.

MRI was performed on a 3T clinical scanner (Philips Achieva, Philips Medical Systems) using a dedicated preclinical asymmetric high-resolution three element receive coil ("Mouse Hotel", Philips), enabling simultaneous measurements of up to 3 animals. Mice were anesthetized with a 10 mL/kg intraperitoneal injection of fentanyl citrate (0.315 mg/mL) plus fluanisone (10 mg/mL; Hypnorm; Janssen Pharmaceutical Ltd.), midazolam (5 mg/mL; Hypnovel; Roche), and water (1:1:2). Anesthetized mice (two per scanning session) were positioned with tumors immobilized at the center of the coil elements (Supplementary Fig. S1). Mouse core body temperature was maintained by a built-in heating system within the coil. A round-end cylinder phantom containing 1.5 mmol/L gadoterate meglumine (Dotarem, Guerbet) in saline was positioned in the third coil element and used to monitor MR system stability (Supplementary Fig. S1). Anatomic coronal and axial  $T_2$ -weighted images were first obtained to localize the tumor. A 2D gradient echo sequence with 6 echo times (temporal resolution: 30 seconds, FA = 24°, TE = 4.92–29.52 ms in increments of 4.92 ms, TR = 250 ms, FOV = 200 × 200 mm<sup>2</sup>, 3 slices, voxel size: 0.3 × 0.3 × 1.5 mm<sup>3</sup>) was then used to scan continuously over 50 minutes, providing 100 time points. The total scanning time was 65 minutes.

### Pathologic assessment of tumor perfusion, vascularization, and hypoxia

The hypoxia marker pimonidazole (60 mg/kg, Hypoxyprobe) was administered intraperitoneally to mice bearing CAL<sup>R</sup> xenografts 1 hour before the MRI scan, to allow for maximal bioreduction in hypoxic tumor regions. Following MRI, Hoechst 33342 (15 mg/kg; Sigma-Aldrich), a marker of perfused vessels, was injected via a lateral tail vein (37, 38). After 1 minute, tumors were rapidly excised and flash frozen over liquid nitrogen. Fluorescence signals from Hoechst 33342 and reduced pimonidazole adducts bound with mouse monoclonal FITC-conjugated antibodies were detected on whole tumor 10- $\mu$ m thick frozen sections, cut in the same plane as for the MRI, using a motorized scanning stage (Prior Scientific Instruments) attached to a BX51 microscope (Olympus Optical), driven by image analysis software (CellP, Soft Imaging System) as

described previously (38). Vessel density was then assessed through detection of CD31 on the same sections using rat anti-mouse CD31 antibodies (BD Biosciences, 1:100) and Alexa 546-conjugated goat anti-rat IgG antibody (Invitrogen, 1:500). Tumor hypoxia, perfusion, and vessel density were quantified as described previously (38).

### Clinical imaging

Ten patients with untreated, histologically proven HNSCC were scanned twice (24–168 hours apart) prior to initiation of treatment. Written informed consent was obtained from all patients, which was approved by the Institutional Research Review Board (CCR 3970) and the NHS Research Ethics Committee (REC number 13/LO/0628). MRI was performed at 3T (MAGNETOM Skyra, Siemens Healthcare) using a 20-channel head and neck coil. Patients were aligned in a supine position with slight neck extension using a standard headrest and lateral cushions for improved stabilization. Anatomic coronal and axial  $T_2$ -weighted images were first acquired to assess the extent of the disease and aid planning of functional imaging. Subsequently, a 2D gradient echo sequence with 6 echo times (temporal resolution: 30 seconds, FA = 24°, TE = 4.92–29.52 ms in increments of 4.92 ms, TR = 250 ms, FOV = 240 × 240 mm<sup>2</sup>, 3 slices, voxel size: 0.9 × 0.9 × 2.5 mm<sup>3</sup>) was used to scan continuously for 1 hour (120 time points). Finally, DCE MRI was performed using an axial 3D FFE sequence (FA = 3/18°, TE/TR = 2.46/4.56 ms, FOV = 256 × 198 mm<sup>2</sup>, 24 slices, 1.5 × 1.5 × 2.5 mm<sup>3</sup> voxel, temporal resolution: 2.9 seconds), during which 0.2 mg/kg gadoterate meglumine was injected as a bolus. The total scanning time was 75 minutes. A blood sample was taken for a full blood count prior to each MRI scan to determine the hematocrit.

### Signal processing

$R_2^*$  maps were calculated for each time point using Matlab (MathWorks), and the gradient echo image signal intensity decay was fitted on a voxel-wise basis to a monoexponential model using a least-squares fit method (30). A nonrigid image registration [MIRT - Medical Image Registration Toolbox for Matlab, sum-of-squared-differences similarity measure (39)] was performed to correct for any motion in the clinical examinations. The shortest echo time (TE = 4.6 ms) images were used to calculate deformation matrices, which were subsequently applied to corresponding  $R_2^*$  maps [ $R_2^*(t)_{MOCO}$ ]. The residual motion was inspected using cine loops and image intensity time traces  $S(t)_{MOCO}$  generated for each tumor volume of interest (50-mm line profiles in two orthogonal directions).

Corrected time series were analyzed for all volumes of interest (VOI) voxels to test for the presence of nonrandom fluctuations, using a power spectrum analysis. The following processing steps, previously described by Baudelet and colleagues (31, 40), were performed: (i) linear trend subtraction; (ii) calculation of autocovariance functions; (iii) calculation of power spectral density; and (iv)  $\chi^2$  test of power coefficients to test whether fluctuations were different from the Gaussian noise. No data filtering or windowing was used. Coefficients in the frequency range of 0 to 0.005 Hz, characteristic for cycling hypoxia (14, 17, 20, 31, 33), were considered significant. Higher frequency noise-dominated coefficients were not included in the analysis. Significant non-Gaussian  $R_2^*$  fluctuations (one or more coefficient above  $P = 0.05$  significance threshold) were spatially mapped using binary maps (Fig. 1).

The total numbers of fluctuating voxels and percentage of fluctuating voxels in the imaged volume (fluctuating volume percentage) were determined for each VOI.

DCE MRI was used to noninvasively investigate the vascularization of the patient tumors. Pharmacokinetic modeling was performed using MRIW (41) software and the extended Kety model (42) and a population-based arterial input function (43). The volume transfer constant between blood plasma and extracellular extravascular space,  $K^{trans}$  (min<sup>-1</sup>), and enhancing fractions, EF, were calculated for each voxel (41).

VOIs from each CAL<sup>R</sup> xenograft were manually delineated using in-house software developed in Matlab. Patient VOIs, including primary and nodal tumor sites, were manually delineated using the Pinnacle3 (Philips Healthcare) treatment planning system (TPS). Voxel-matched parameter maps were generated and exported using the TPS with 1 × 1 × 2.5 mm voxel resolution. This allowed for spatial investigation of perfusion and permeability in fluctuating and nonfluctuating tumor regions. Mean values of  $R_2^*$  and  $K^{trans}$  were calculated for enhancing regions of tumors and compared with fluctuating and nonfluctuating subvolumes. Correlations between whole tumor median  $K^{trans}$ ,  $R_2^*$  VOI values, and fluctuating volume percentage were also tested.

### Treatment and outcomes in the clinical cohort

All patients received radical radiotherapy with concomitant chemotherapy (cisplatin 100 mg/m<sup>2</sup> or carboplatin, AUC5, day 1 and 29) according to institutional protocols. Macroscopic and microscopic disease received 65 or 54 Gy in 30 fractions, respectively, using intensity-modulated radiotherapy with a simultaneous integrated boost. Macroscopic disease was defined as the gross tumor identifiable on pretreatment images and clinical examination, whereas microscopic disease included nodal areas at risk of harboring microscopic disease dependent on the site of the primary tumor. Patients with evidence of persistent, progressive, or relapsed disease, arising within 12 months of completion of treatment, were classed as nonresponders. The analysis of the clinical MRI data was blinded to the treatment outcome.

### Statistical analysis

The Shapiro-Wilk test was used to evaluate distribution normality of measured parameters. The  $\chi^2$  test of power coefficients (frequency range, 0–0.005 Hz) was used to assess whether the fluctuations were different from the Gaussian noise. The paired  $t$  test was used to compare the mean values of  $R_2^*$ ,  $K^{trans}$  (responders vs. nonresponders, primary vs. lymph nodal tumors), and fluctuating volume percentage (responders vs. nonresponders, fluctuating volume percentage in MR1 vs. MR2). Kendall tau ( $\tau$ ) was used to test for correlation between the mean fluctuating volume percentage,  $R_2^*$ , and vascular/hypoxia parameters (Hoechst 33342, pimonidazole adduct fractions,  $K^{trans}$ ). A  $P$  value of 0.05 was chosen as the criterion for statistical significance in all tests and adjusted to account for multiple correlation comparisons. Statistical analysis was performed using the Matlab Statistics Toolbox.

## Results

### Preclinical findings

*The spatial distribution and volume percentage of spontaneous  $R_2^*$  fluctuations.* The range of CAL<sup>R</sup> tumor volumes measured

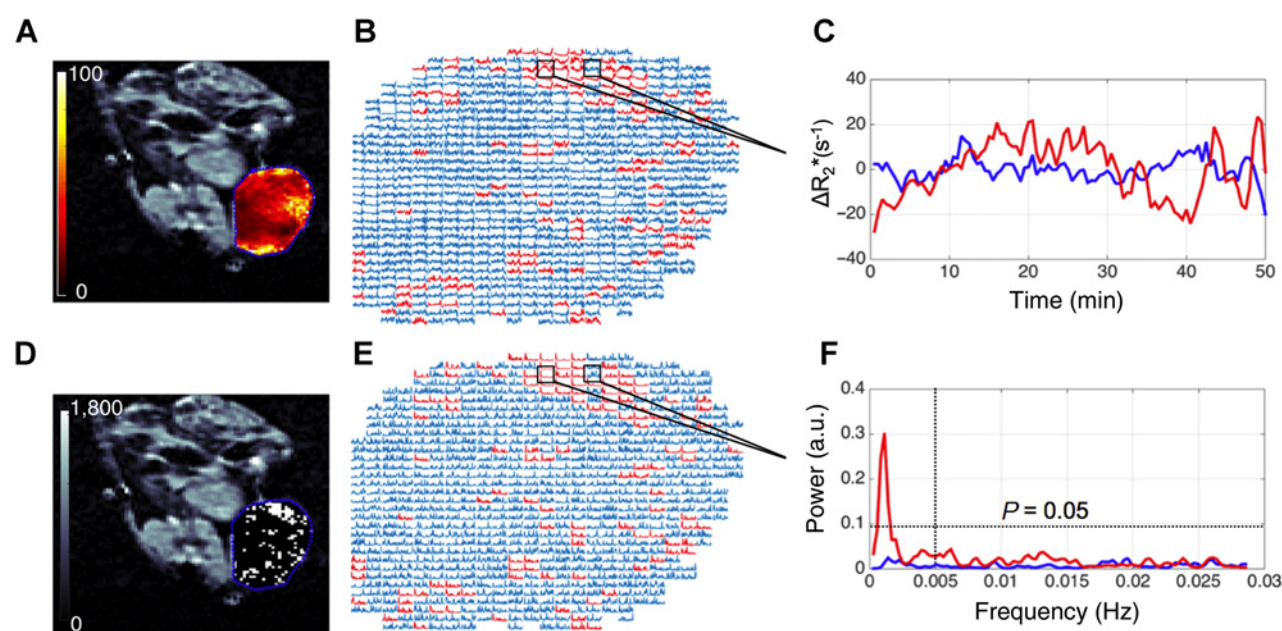


**Figure 1.** **A**, Representative parametric  $R_2^*$  map (range, 0–100  $s^{-1}$ , axial orientation) calculated for a CAL<sup>R</sup> HNSCC xenograft, with the tumor ROI delineated in blue.  $R_2^*$  time series (**B** and **C**) were used to calculate corresponding power spectra (**E** and **F**) and tested for the presence of nonrandom fluctuations. Significant non-Gaussian  $R_2^*$  fluctuations (white voxels in binary maps **D**), in the frequency range of 0 to 0.005 Hz were spatially mapped ( $\chi^2$  test: at least one coefficient above  $P = 0.05$ , **E** and **F**).

using  $T_2$ -weighted images was 0.48 to 0.94  $cm^3$  with a median of 0.59  $cm^3$ . The median baseline  $R_2^*$  for the CAL<sup>R</sup> xenografts was 32  $s^{-1}$  (range: 26–50  $s^{-1}$ ) with elevated values commonly found at the periphery of tumors (Fig. 1A). Significant spontaneous  $R_2^*$  spatial variations were detected in all the CAL<sup>R</sup> xenografts ( $n = 5$ ), with an average fluctuating volume percentage of 8% (Table 1). Figure 2B illustrates the spatial distribution of fluctuations in the xenograft cohort. Examples of power spectra measured for representative voxels in fluctuating and nonfluctuating regions of CAL<sup>R</sup> xenografts, and adjacent muscle, are shown in Supplementary Fig. S2.

**Perfusion and hypoxia in fluctuating subregions of CAL<sup>R</sup> xenografts.** Composite images showing the distribution of Hoechst 33342, pimonidazole adducts, and CD31 for each CAL<sup>R</sup> xenograft are shown in Fig. 2C. Perfused vasculature was predominantly associated with the tumor periphery, with more hypoxic and/or avascular regions toward the core. The mean values of perfused and hypoxic fractions were 10.4% (range, 5.1–14.2) and 7% (range, 6.5–20.9), respectively.

There was a negative trend ( $\tau = -0.8$ ,  $P = 0.08$ , Supplementary Fig. S3) between median-fluctuating and perfused tumor

fractions. There was no correlation between median-fluctuating volume percentage and chronic hypoxia, identified with pimonidazole staining ( $\tau = -0.2$ ,  $P = 0.817$ ). Significant  $R_2^*$  fluctuations were apparent in regions of the tumor with a heterogeneous distribution of hypoxic and perfused parts, although absent in well-perfused areas (Fig. 2B). There was no correlation between baseline  $R_2^*$  and pimonidazole or Hoechst 33342 staining ( $\tau = 0.1$ ,  $P = 1$  and  $\tau = 0.01$ ,  $P = 1$ , respectively, Supplementary Fig. S3).

**Clinical findings**

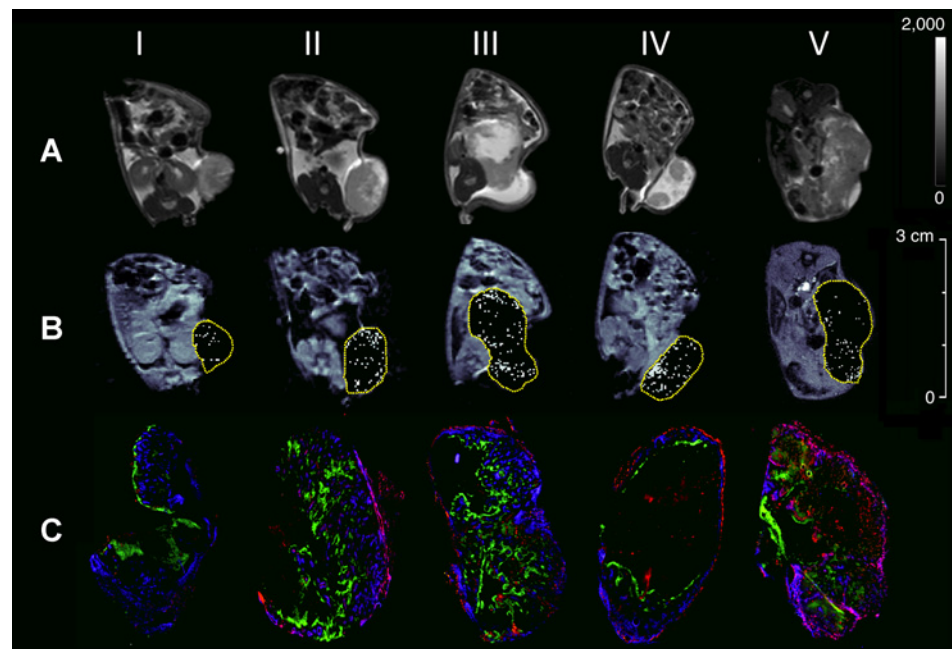
**The spatial distribution and volume percentage of spontaneous  $R_2^*$  fluctuations.** A total of 7 primary sites and 11 lymph nodes were imaged and outlined for the purpose of the study. Patient and treatment characteristics are summarized in Table 2. The range of measured Hct was 0.283 to 0.459, and the mean value was 0.4. Images revealed high spatial heterogeneity in metastatic lymph nodes (Fig. 3). The median baseline  $R_2^*$  was 43  $s^{-1}$  (range: 35–56  $s^{-1}$ ) for lymph nodes and 54  $s^{-1}$  (range, 47–56  $s^{-1}$ ) for primary tumors, which differed significantly ( $P < 0.01$ ). Elevated  $R_2^*$  values were commonly found at the periphery of lymph nodes (Fig. 4A). Primary sites were significantly

**Table 1.** Summary of CAL<sup>R</sup> tumor characteristics

Mouse no.	Tumor volume (cc)	H33342 fraction (%)	Pimonidazole fraction (%)	$R_2^*$ ( $s^{-1}$ )	Fluctuating volume (%)
1	0.41	14	7	32	4
2	0.48	10	17	50	10
3	0.94	13	21	26	7
4	0.59	5	2	27	11
5	0.92	8	7	34	8
Median	0.59	10	7	32	8

**Figure 2.**

**A and B,** T<sub>2</sub>-weighted axial MRI images (**A**) and corresponding binary maps showing the spatial distribution of spontaneous non-Gaussian R<sub>2</sub><sup>\*</sup> fluctuations (**B**) within tumor ROIs (white voxels) for CAL<sup>R</sup> HNSCC xenografts (central slices). **C,** Composite images of the corresponding tumor sections showing the distribution of Hoechst 33342 (perfusion, blue), pimonidazole adducts (hypoxia, green), and CD31 (endothelial cell expression, red).



affected by patient motion, whereas lymph nodes were fairly stationary (Supplementary Fig. S4). Three primary tumors were excluded from the analysis due to excessive motion that could not be compensated for. Significant R<sub>2</sub><sup>\*</sup> fluctuations were detected in 4 primary sites and 10 lymph nodes in 9 of 10 patients, with the fluctuating volume percentage varying between 0% and 23% (Table 2). Examples of nodal VOI fluctuation maps obtained in two MRI sessions (48 hours apart) are shown in Fig. 4. Examples of power spectra measured for representative voxels in fluctuating and nonfluctuating parts of human HNSCC tumors, and adjacent muscle, are shown in Supplementary Fig. S5.

Mean values of fluctuating volume percentage measured in the two MRI visits did not differ statistically ( $P = 0.12$ ).

The distribution of fluctuating volume percentage in the patient cohort was positively skewed and not normal ( $P < 0.01$ ). Most of

the observed significant frequencies were in the low-frequency range  $< 0.003$  Hz ( $< 1$  cycle/5.5 minutes) with a median frequency of 0.0011 Hz (1 cycle/15 minutes).

**K<sup>trans</sup> and R<sub>2</sub><sup>\*</sup> in fluctuating and nonfluctuating parts of patient tumors.** The median K<sup>trans</sup> values calculated for patient primary and nodal tumors were 0.127 and 0.182 min<sup>-1</sup>, respectively. A rim-enhancing pattern, with no or low contrast uptake in the center, was observed in 7 of 11 nodes. The mean nodal-enhancing fraction was 0.86. There was no difference in enhancing fraction values between fluctuating and nonfluctuating parts of nodal tumors ( $P = 0.84$ ). Examples of fluctuation maps with corresponding K<sup>trans</sup> maps are shown in Figs. 3 and 4. Nonrandom fluctuations were detected in areas of lymph nodes with low K<sup>trans</sup> values (Figs. 3, IV and Fig. 4), often in the vicinity, but not in the center, of cystic or necrotic

**Table 2.** Summary of patient tumor characteristics

Pt	Primary site	Primary tumors					Lymph nodes					Outcome
		P vol (cc)	R <sub>2</sub> <sup>*</sup> (s <sup>-1</sup> )	K <sup>trans</sup> (min <sup>-1</sup> )	MR1 Fluct. vol. (%)	MR2 Fluct. vol. (%)	LN vol (cc)	R <sub>2</sub> <sup>*</sup> (s <sup>-1</sup> )	K <sup>trans</sup> (min <sup>-1</sup> )	MR1 Fluct. vol. (%)	MR2 Fluct. vol. (%)	
1	Oropharynx	12	50	0.153	1	4	15	52	0.264	1	1	R
2	Oropharynx	32	54	0.079	NA	NA	2	51	0.186	2	10	R
3	Supraglottis	27	54	0.135	NA	NA	3	38	0.046	0	0	NR
4	Oropharynx	29	47	0.112	2	1	2	42	0.277	4	6	R
5	Oropharynx	173	54	0.147	0	2	6	48	0.129	8	23	NR
							2	44	0.102	14	8	
6	Supraglottis	12	56	0.145	NA	NA	15	43	0.215	3	1	NR
7	Oropharynx	—	—	—	—	—	5	38	0.139	7	5	NR
8	Supraglottis	—	—	—	—	—	10	35	0.242	2	8	R
							15	41	0.346	1	4	
9	Oropharynx	—	—	—	—	—	17	45	0.060	1	2	R
10	Oropharynx	45	56	0.117	1	4	—	—	—	—	—	R
	Median	28	54	0.135	1	3	5	43	0.186	2	5	

NOTE: "—": no primary/lymph node in the imaged volume.

Abbreviations: NA, data not available due to extensive motion; R/NR, responder/nonresponder.

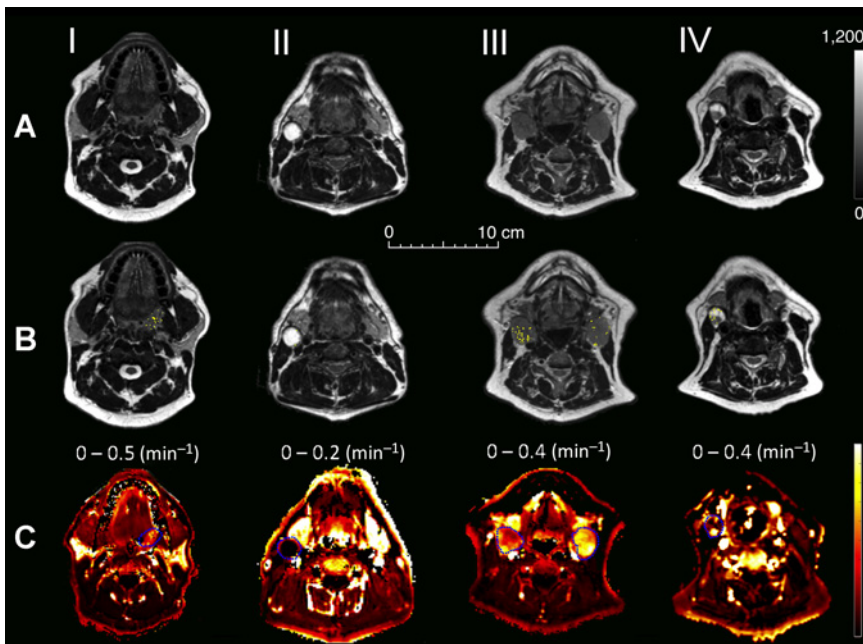


**Figure 3.**  
**A.** Examples of T<sub>2</sub>-weighted axial MRI images of HNSCC patients. The distribution of spontaneous R<sub>2</sub><sup>\*</sup> fluctuations (**B**) within tumor ROIs (white voxels) is presented for a primary tumor site (I, Pt no.: 1), necrotic node (II, Pt no.: 2) uniformly and nonuniformly contrast-enhancing nodes (III, Pt no.: 8 and IV, Pt no.: 7). **C.** Corresponding K<sup>trans</sup> maps showing distribution of volume transfer constant between blood plasma and extracellular extravascular space.

nodes (Fig. 3II). Mean K<sup>trans</sup> values were lower in the fluctuating regions of nodal tumors ( $P < 0.01$ ) and baseline R<sub>2</sub><sup>\*</sup> values did not differ ( $P = 0.97$ ). There was no correlation between mean K<sup>trans</sup> or R<sub>2</sub><sup>\*</sup> and fluctuating volume percentage ( $\tau = -0.09$ ,  $P = 0.75$  and  $\tau = 0.06$ ,  $P = 0.87$ , respectively) in the lymph nodes (representative K<sup>trans</sup> and R<sub>2</sub><sup>\*</sup> distributions for fluctuating and nonfluctuating human HNSCC tumor regions are shown in Supplementary Fig. S6).

**Treatment outcomes.** Clinical outcomes are presented in Table 2. Six of 10 patients were classified as responders, while 3 patients developed progressive or residual disease 3 months postcompletion of the treatment (Pt 3, 5, 7). One patient had locoregional disease relapse 9 months postcompletion of the treatment (Pt 5). The mean lymph nodes fluctuating volume percentage, averaged for both visits, was 8% (range, 2%–15%) in nonresponders and 3% (range, 0%–6%) in responders (Supplementary Fig. S7). The

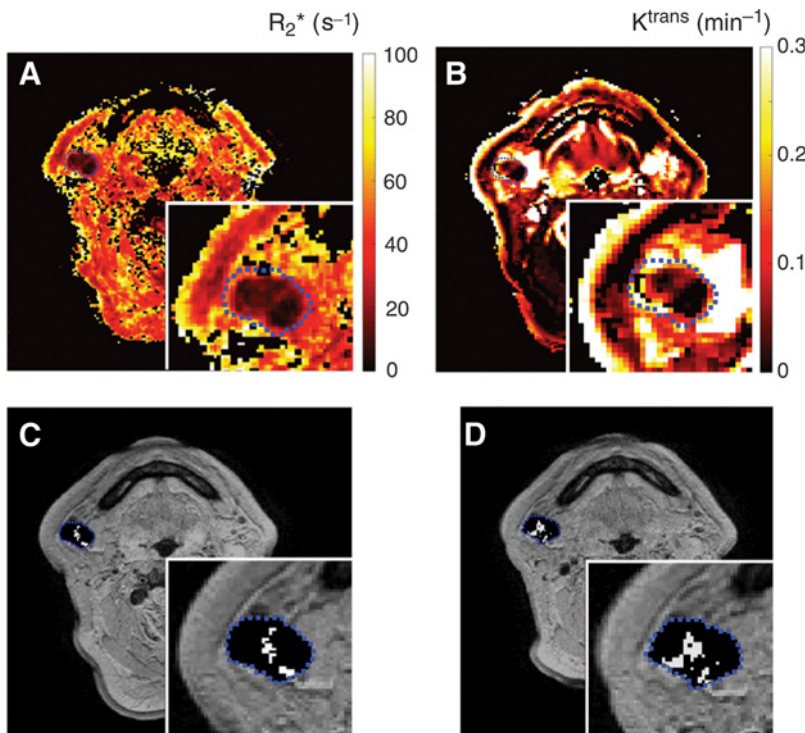


**Figure 4.**  
 MRI parametric maps for a stage IV HNSCC patient with a zoomed nodal ROI region. **A–D.** Transverse relaxation rate R<sub>2</sub><sup>\*</sup> (**A**), K<sup>trans</sup> (**B**), and binary maps [MR1 (**C**), MR2 (**D**), two MR sessions 48 hours apart] showing spatial distribution of spontaneous non-Gaussian R<sub>2</sub><sup>\*</sup> fluctuations (white voxels) for a nodal ROI (patient no. 5, N2).

Downloaded from <http://aacrjournals.org/clinccancerres/article-pdf/23/15/4233/204077/4233.pdf> by guest on 12 September 2022

difference was borderline insignificant ( $P = 0.051$ ). There were insufficient data for the primary tumor analysis. There was no difference in mean tumor  $K^{\text{trans}}$  ( $P_{\text{primary}} = 0.19$ ,  $P_{\text{nodes}} = 0.96$ ) or  $R_2^*$  ( $P_{\text{primary}} = 0.29$ ,  $P_{\text{nodes}} = 0.81$ ) values between responders and nonresponders.

## Discussion

In this study, we describe the successful implementation of IS-MRI for noninvasive imaging of cycling oxygenation changes in HNSCC, using a clinical 3T MRI scanner. Following promising results from the preclinical phase, the methodology was translated to a clinical study. To the best of our knowledge, our study is the first application of serial IS-MRI methodology to detect cycling hypoxia in a clinical setting.

Measurements of cycling hypoxia using serial IS-MRI was first introduced in a preclinical study of murine fibrosarcoma performed at 4.7T by Baudalet and colleagues (31, 40). In our study, spontaneous  $R_2^*$  fluctuations, reflecting varying blood flow and levels of oxygenation/hypoxia, were detected in both CAL<sup>R</sup> xenografts and patients with HNSCC. Preclinically, the cycling variations were apparent in mixed perfused and hypoxic regions of the tumor, confirmed histologically using Hoechst 33342 uptake, and pimonidazole adduct formation. In the patients,  $R_2^*$  fluctuations were observed within areas of lymph nodes exhibiting low  $K^{\text{trans}}$  values, often in the vicinity, but not in the center, of necrotic nodes. It has previously been shown that  $K^{\text{trans}}$  values correlate with the level of perfusion (42). We observed lower  $K^{\text{trans}}$  values in fluctuating parts of metastatic lymph nodes, which suggest that fluctuating blood oxygen levels are caused by an insufficient or intermittent blood delivery as a result of aberrant vasculature. This observation aligns with another preclinical study in which approximately 80% of the fluctuations were found to occur in tumor regions with immature vessels (44). This may underpin the negative trend observed between fluctuating  $R_2^*$  and perfused fraction in the CAL<sup>R</sup> xenografts, and the negligible level of fluctuations detected within chronically hypoxic and avascular tumor areas identified by pimonidazole adduct formation and DCE MRI, respectively. The lack of correlation between pimonidazole,  $K^{\text{trans}}$ , and fluctuating volume percentage also indicates that regions exhibiting intermittent blood flow and cycling hypoxia cannot be detected using single contrast agent injection methods. The bioreduction of pimonidazole is averaged in time postinjection and therefore not sensitive to acute changes of hypoxia. DCE data are acquired typically over a much shorter period of time (<10 minutes), and pharmacokinetic modeling assumes constant rates of perfusion and permeability in the assessed vasculature. Serial IS-MRI can be acquired over a longer period of time, revealing the presence of oxygen level fluctuations at frequencies characteristic of cycling hypoxia.

Frequencies in the range of 0.00027 to 0.001 Hz (15–60 minutes) have been reported in preclinical measurements of cycling hypoxia (14, 17, 20, 31, 33). The median frequency of 0.0011 Hz (1 cycle/15 minutes) found in our study is comparable with tumor  $R_2^*$  oscillation frequencies reported by Baudalet and colleagues and Goncalves and colleagues (0.0036 Hz and <0.001 Hz, respectively; refs. 31, 33).

CAL<sup>R</sup> xenografts were used in this study, as they emulate the high vascular heterogeneity frequently found in HNSCC tumors in the clinic. It is expected that blood volume is higher in primary HNSCC tumors than metastatic lymph nodes, which

for comparable level of tissue oxygenation would result in faster  $R_2^*$  rates (more paramagnetic deoxyHb/voxel; refs. 30, 45). Similarly, in the case of severely hypoxic hypovascular tissues, such as those observed in CAL<sup>R</sup> tumors, slow values of  $R_2^*$  would be predicted. The presence of hypoxic and underperfused tumor subregions, characteristic of CAL<sup>R</sup> tumors (37), has also been reported in patients with metastatic HNSCC lymph nodes (46). This is consistent with our findings of abundant regions of impaired perfusion and necrosis identified in both preclinical and clinical settings. In our study, the median-fluctuating volume percentage, detected in all imaged CAL<sup>R</sup> tumors, was 8% (range, 4%–11%). This was comparable, but did not correlate ( $\tau = -0.2$ ,  $P = 0.817$ ), with the pimonidazole fraction (7%). The incidence of cyclical hypoxia is more likely in tumor regions where the oxygen saturation of the blood entering that region is relatively low, resulting in a complex dynamic interplay between chronic and cyclical hypoxia (18). The levels of fluctuating and hypoxic fractions depend on the tumor type, presence of necrosis, vascular stability, and oxygen consumption. The fluctuating volume percentage has also been shown to depend on the study methodology, with published estimates varying between 0% and 80% (17).

Noninvasive measurement of cycling tumor hypoxia is challenging in patients due to the need for multiple data time points. Most of the methodologies that have been successfully used to study varying levels of hypoxia in preclinical studies are not applicable to clinical studies. Invasive studies of superficial human tumors using laser Doppler flow measurement demonstrated significant changes in microregional blood flow in 54% of the regions monitored over a 60-minute period (47, 48). Around 19% of the observed perfusion changes were reversed over a time course of 4 to 44 minutes. A modeling study using serial pretreatment <sup>18</sup>F-FMISO-PET scans in patients with HNSCC reported that acute hypoxia ranged from 13% to 52% (49). In our study, fluctuating volume percentage varied between 0 and 23%. The level of fluctuations was consistent between the scans: mean values of fluctuating volume percentage measured in two MRI visits did not differ statistically ( $P = 0.12$ ), confirming robustness of methodology and prevalence of cycling oxygenation changes in HNSCC tumors. Assuming the average patient value of systemic hematocrit (0.4) as the value of microvascular hematocrit, and a hypoxic range of blood oxygenation between 0 and 0.3, the maximum observed  $\Delta R_2^*$  ( $\sim 40 \text{ s}^{-1}$ ) would correspond to a 0.2 change in blood oxygenation at 3T (45). This would equate to a change of between 0 and 16 mm Hg (human blood, coefficient for blood oxygen binding: 2.26, temperature: 37°C, pH: 7.4).

Intriguingly, the difference of the mean fluctuating volume percentage between responding and nonresponding patient groups approached statistical significance ( $P = 0.051$ ), indicating the potential of  $R_2^*$  fluctuating volume percentage as a predictive and prognostic biomarker in HNSCC. This warrants further evaluation in a larger patient group.

Several limitations of this study should be considered. Patient HNSCC primary tumor sites (e.g., base of tongue, pharynx) were affected by significant internal motion that could not be compensated for and hence led to exclusion from the analysis. One possible way to reduce this issue would be to use customized oral stents (50). This may decrease patient comfort however, and the tolerability would have to be assessed. Another limitation is the restricted coverage of the serial multiple gradient echo at the required temporal resolution. This limited our

analysis to the center part of primary tumors and coplanar local lymph nodes. Echo planar imaging readouts, commonly used in serial IS-MRI studies of brain activity, may improve this aspect (51). These sequences are, however, prone to distortion artifacts in the vicinity of air and tissue interfaces, which is likely to affect HNSCC primary tumor analysis (52). Finally, the prevalence and spatial distribution of oxygen fluctuation in patients was correlated to the transfer constant  $K^{trans}$  estimated using DCE MRI, but not to the absolute level of chronic hypoxia, which is a common and well-recognized cause of radioresistance in HNSCC. MRI-based methods to identify chronic hypoxia employing hyperoxic challenge-induced changes in  $R_2^*$  and  $R_1$  have recently been proposed (53–55) and could be combined with serial IS-MRI in future studies to provide information on the impact of both cycling and chronic hypoxia on patient treatment.

In conclusion, we demonstrated the feasibility of oxygen fluctuation mapping in HNSCC xenografts and translation to patient tumors using a clinical 3T MRI system. Our results suggest the presence of fluctuating blood oxygen levels in regions of impaired vasculature, but not in necrotic avascular parts of the tumor.

#### Disclosure of Potential Conflicts of Interest

No potential conflicts of interest were disclosed.

#### Authors' Contributions

**Conception and design:** M. Leach, L. Baker, K. Harrington, D. Koh, K. Newbold, C. Nutting, R. Panek, S. Robinson, L. Welsh

**Development of methodology:** L. Baker, A. Dunlop, K. Newbold, C. Nutting, R. Panek, M. Schmidt, L. Welsh

**Acquisition of data (provided animals, acquired and managed patients, provided facilities, etc.):** S. Bhide, C. Box, A. Dunlop, K. Harrington, G. Hopkinson, K. Newbold, C. Nutting, R. Panek, C. Richardson, S. Robinson, L. Welsh, K. Wong

**Analysis and interpretation of data (e.g., statistical analysis, biostatistics, computational analysis):** L. Baker, A. Dunlop, K. Harrington, D. McQuaid, K. Newbold, C. Nutting, R. Panek, A. Riddell, M. Schmidt, L. Welsh, K. Wong

**Writing, review, and/or revision of the manuscript:** M. Leach, L. Baker, S. Bhide, C. Box, J. d'Arcy, A. Dunlop, S. Eccles, K. Harrington, D. Koh, K. Newbold, C. Nutting, R. Panek, C. Richardson, A. Riddell, S. Robinson, M. Schmidt, L. Welsh, K. Wong

**Administrative, technical, or material support (i.e., reporting or organizing data, constructing databases):** L. Baker, J. d'Arcy, D. McQuaid, C. Richardson, K. Wong

**Study supervision:** M. Leach, K. Harrington, K. Newbold, C. Nutting, S. Robinson

#### Acknowledgments

The authors would like to thank Jessica Boulton and Yann Jamin for constructive discussions, the MRI team at the Royal Marsden Hospital, and staff from the Biological Services Unit for their help.

#### Grant Support

This work was supported by Cancer Research UK Programme Grants C46/A10588 and C7224/A13407. The authors also acknowledge the support of CRUK and EPSRC to the Cancer Imaging Centre at ICR and RMH in association with MRC & Department of Health C1060/A10334, C1060/A16464 CRUK project grant C1060/A12752 and MRC grant G0701533, together with funding to the RM/ICR NIHR Biomedical Research Centre and the Clinical Research Facility in Imaging. M.O. Leach and K.J. Harrington are NIHR Senior Investigators. C. Box was supported by the Oracle Cancer Trust. This work was undertaken at The Royal Marsden NHS Foundation Trust, which received a proportion of its funding from the NHS Executive. The views expressed in this publication are those of the authors and not necessarily those of the NHS Executive.

The costs of publication of this article were defrayed in part by the payment of page charges. This article must therefore be hereby marked *advertisement* in accordance with 18 U.S.C. Section 1734 solely to indicate this fact.

Received May 11, 2016; revised July 19, 2016; accepted March 3, 2017; published OnlineFirst March 17, 2017.

#### References

- Brown JM. Tumor microenvironment and the response to anticancer therapy. *Cancer Biol Ther* 2002;1:453–8.
- Horsman MR, Mortensen LS, Petersen JB, Busk M, Overgaard J. Imaging hypoxia to improve radiotherapy outcome. *Nat Rev Clin Oncol* 2012;9:674–87.
- Barker HE, Paget JT, Khan AA, Harrington KJ. The tumour microenvironment after radiotherapy: mechanisms of resistance and recurrence. *Nat Rev Cancer* 2015;15:409–25.
- Brown JM. Tumor hypoxia in cancer therapy. *Methods Enzymol* 2007;435:297–321.
- Harada H. How can we overcome tumor hypoxia in radiation therapy? *J Radiat Res* 2011;52:545–56.
- Brizel DM, Sibley GS, Prosnitz LR, Scher RL, Dewhirst MW. Tumor hypoxia adversely affects the prognosis of carcinoma of the head and neck. *Int J Radiat Oncol Biol Phys* 1997;38:285–9.
- Overgaard J, Horsman MR. Modification of hypoxia-induced radioresistance in tumors by the use of oxygen and sensitizers. *Semin Radiat Oncol* 1996;6:10–21.
- Overgaard J. Hypoxic modification of radiotherapy in squamous cell carcinoma of the head and neck—a systematic review and meta-analysis. *Radiother Oncol* 2011;100:22–32.
- Thomlinson RH, Gray LH. The histological structure of some human lung cancers and the possible implications for radiotherapy. *Br J Cancer* 1955;9:539–49.
- Trotter MJ, Acker BD, Chaplin DJ. Histological evidence for nonperfused vasculature in a murine tumor following hydralazine administration. *Int J Radiat Oncol Biol Phys* 1989;17:785–9.
- Lunt SJ, Chaudary N, Hill RP. The tumor microenvironment and metastatic disease. *Clin Exp Metastasis* 2009;26:19–34.
- Bristow RG, Hill RP. Hypoxia and metabolism. Hypoxia, DNA repair and genetic instability. *Nat Rev Cancer* 2008;8:180–92.
- Brown JM. Evidence for acutely hypoxic cells in mouse tumours, and a possible mechanism of reoxygenation. *Br J Radiol* 1979;52:650–6.
- Chaplin DJ, Durand RE, Olive PL. Acute hypoxia in tumors: implications for modifiers of radiation effects. *Int J Radiat Oncol Biol Phys* 1986;12:1279–82.
- Chaplin DJ, Olive PL, Durand RE. Intermittent blood flow in a murine tumor: radiobiological effects. *Cancer Res* 1987;47:597–601.
- Bayer C, Shi K, Astner ST, Mafei CA, Vaupel P. Acute versus chronic hypoxia: why a simplified classification is simply not enough. *Int J Radiat Oncol Biol Phys* 2011;80:965–8.
- Bayer C, Vaupel P. Acute versus chronic hypoxia in tumors: controversial data concerning time frames and biological consequences. *Strahlenther Onkol* 2012;188:616–27.
- Dewhirst MW. Relationships between cycling hypoxia, HIF-1, angiogenesis and oxidative stress. *Radiat Res* 2009;172:653–65.
- Lanzen J, Braun RD, Klitzman B, Brizel D, Secomb TW, Dewhirst MW. Direct demonstration of instabilities in oxygen concentrations within the extravascular compartment of an experimental tumor. *Cancer Res* 2006;66:2219–23.
- Dewhirst MW, Kimura H, Rehmus SW, Braun RD, Papahadjopoulos D, Hong K, et al. Microvascular studies on the origins of perfusion-limited hypoxia. *Br J Cancer Suppl* 1996;27:S247–51.

21. Intaglietta M, Myers RR, Gross JF, Reinhold HS. Dynamics of microvascular flow in implanted mouse mammary tumours. *Bibl Anat* 1977 (15 Pt 1):273–6.
22. Patan S, Munn LL, Jain RK. Intussusceptive microvascular growth in a human colon adenocarcinoma xenograft: a novel mechanism of tumor angiogenesis. *Microvasc Res* 1996;51:260–72.
23. Dewhirst MW. Concepts of oxygen transport at the microcirculatory level. *Semin Radiat Oncol* 1998;8:143–50.
24. Kiani MF, Pries AR, Hsu LL, Sarelius IH, Cokelet GR. Fluctuations in microvascular blood flow parameters caused by hemodynamic mechanisms. *Am J Physiol* 1994;266(5 Pt 2):H1822–8.
25. Mollica F, Jain RK, Netti PA. A model for temporal heterogeneities of tumor blood flow. *Microvasc Res* 2003;65:56–60.
26. Hammond EM, Kaufmann MR, Giaccia AJ. Oxygen sensing and the DNA-damage response. *Curr Opin Cell Biol* 2007;19:680–4.
27. Klein TJ, Glazer PM. The tumor microenvironment and DNA repair. *Semin Radiat Oncol* 2010;20:282–7.
28. Baudelet C, Gallez B. How does blood oxygen level-dependent (BOLD) contrast correlate with oxygen partial pressure (pO<sub>2</sub>) inside tumors? *Magn Resonance Med* 2002;48:980–6.
29. Neeman M, Dafni H, Bukhari O, Braun RD, Dewhirst MW. *In vivo* BOLD contrast MRI mapping of subcutaneous vascular function and maturation: validation by intravital microscopy. *Magn Reson Med* 2001;45:887–98.
30. Panek R, Welsh L, Dunlop A, Wong KH, Riddell AM, Koh DM, et al. Repeatability and sensitivity of T<sub>2</sub>\* measurements in patients with head and neck squamous cell carcinoma at 3T. *J Magn Resonance Imaging* 2016;44:72–80.
31. Baudelet C, Ansiaux R, Jordan BF, Havaux X, Macq B, Gallez B. Physiological noise in murine solid tumours using T<sub>2</sub>\*-weighted gradient-echo imaging: a marker of tumour acute hypoxia? *Phys Med Biol* 2004;49:3389–411.
32. Fru LC, Adamson EB, Campos DD, Fain SB, Jacques SL, van der Kogel AJ, et al. Potential role of the glycolytic oscillator in acute hypoxia in tumors. *Phys Med Biol* 2015;60:9215–25.
33. Goncalves MR, Johnson SP, Ramasawmy R, Pedley RB, Lythgoe MF, Walker-Samuel S. Decomposition of spontaneous fluctuations in tumour oxygenation using BOLD MRI and independent component analysis. *Br J Cancer* 2015;113:1168–77.
34. Workman P, Aboagye EO, Balkwill F, Balmain A, Bruder G, Chaplin DJ, et al. Guidelines for the welfare and use of animals in cancer research. *Br J Cancer* 2010;102:1555–77.
35. Kilkenny C, Browne WJ, Cuthill IC, Emerson M, Altman DG. Improving bioscience research reporting: the ARRIVE guidelines for reporting animal research. *J Pharmacol Pharmacother* 2010;1:94–9.
36. Box C, Mendiola M, Gowen S, Box GM, Valenti M, Brandon Ade H, et al. A novel serum protein signature associated with resistance to epidermal growth factor receptor tyrosine kinase inhibitors in head and neck squamous cell carcinoma. *Eur J Cancer* 2013;49:2512–21.
37. Baker LCJ, Box C, Sikka A, Box G, Eccles SA, Robinson SP. Evaluating imaging biomarkers of acquired resistance to targeted EGFR therapy in xenograft models of human squamous cell carcinoma of the head and neck (SCCHN) [abstract]. In: Proceedings of the 104th Annual Meeting of the American Association for Cancer Research; 2013 Apr 6–10; Washington, DC. Philadelphia, PA: AACR; 2013. Abstract nr 4459.
38. Boulton JK, Walker-Samuel S, Jamin Y, Leiper JM, Whitley GS, Robinson SP. Active site mutant dimethylarginine dimethylaminohydrolase 1 expression confers an intermediate tumour phenotype in C6 gliomas. *J Pathol* 2011;225:344–52.
39. Myronenko A, Song X. Intensity-based image registration by minimizing residual complexity. *IEEE Trans Med Imaging* 2010;29:1882–91.
40. Baudelet C, Gallez B. Cluster analysis of BOLD fMRI time series in tumors to study the heterogeneity of hemodynamic response to treatment. *Magn Reson Med* 2003;49:985–90.
41. d'Arcy JA, Collins DJ, Padhani AR, Walker-Samuel S, Suckling J, Leach MO. Informatics in Radiology (infoRAD): magnetic resonance imaging workbench: analysis and visualization of dynamic contrast-enhanced MR imaging data. *Radiographics* 2006;26:621–32.
42. Tofts PS, Brix G, Buckley DL, Evelhoch JL, Henderson E, Knopp MV, et al. Estimating kinetic parameters from dynamic contrast-enhanced T<sub>1</sub>-weighted MRI of a diffusible tracer: standardized quantities and symbols. *J Magn Reson Imaging* 1999;10:223–32.
43. Orton MR, d'Arcy JA, Walker-Samuel S, Hawkes DJ, Atkinson D, Collins DJ, et al. Computationally efficient vascular input function models for quantitative kinetic modelling using DCE-MRI. *Phys Med Biol* 2008;53:1225–39.
44. Baudelet C, Cron GO, Ansiaux R, Crokart N, DeWever J, Feron O, et al. The role of vessel maturation and vessel functionality in spontaneous fluctuations of T<sub>2</sub>\*-weighted GRE signal within tumors. *NMR Biomed* 2006;19:69–76.
45. Zhao JM, Clingman CS, Närviäinen MJ, Kauppinen RA, van Zijl PC. Oxygenation and hematocrit dependence of transverse relaxation rates of blood at 3T. *Magn Reson Med* 2007;58:592–7.
46. Newbold K, Castellano I, Charles-Edwards E, Mears D, Sohaib A, Leach M, et al. An exploratory study into the role of dynamic contrast-enhanced magnetic resonance imaging or perfusion computed tomography for detection of intratumoral hypoxia in head-and-neck cancer. *Int J Radiat Oncol Biol Phys* 2009;74:29–37.
47. Pigott KH, Hill SA, Chaplin DJ, Saunders MI. Microregional fluctuations in perfusion within human tumours detected using laser Doppler flowmetry. *Radiation Oncol* 1996;40:45–50.
48. Powell ME, Hill SA, Saunders MI, Hoskin PJ, Chaplin DJ. Human tumor blood flow is enhanced by nicotinamide and carbogen breathing. *Cancer Res* 1997;57:5261–4.
49. Wang K, Yorke E, Nehmeh SA, Humm JL, Ling CC. Modeling acute and chronic hypoxia using serial images of 18F-FMISO PET. *Med Phys* 2009;36:4400–8.
50. Johnson B, Sales L, Winston A, Liao J, Laramore G, Parvathaneni U. Fabrication of customized tongue-displacing stents: considerations for use in patients receiving head and neck radiotherapy. *J Am Dent Assoc* 2013;144:594–600.
51. Mark CI, Mazerolle EL, Chen JJ. Metabolic and vascular origins of the BOLD effect: implications for imaging pathology and resting-state brain function. *J Magn Reson Imaging* 2015;42:231–46.
52. Schouten CS, de Bree R, van der Putten L, Noij DP, Hoekstra OS, Comans EF, et al. Diffusion-weighted EPI- and HASTE-MRI and 18F-FDG-PET-CT early during chemoradiotherapy in advanced head and neck cancer. *Quant Imaging Med Surg* 2014;4:239–50.
53. Hallac RR, Zhou H, Pidikiti R, Song K, Stojadinovic S, Zhao D, et al. Correlations of noninvasive BOLD and TOLD MRI with pO<sub>2</sub> and relevance to tumor radiation response. *Magn Reson Med* 2014;71:1863–73.
54. O'Connor JP, Boulton JK, Jamin Y, Babur M, Finegan KG, Williams KJ, et al. Oxygen-enhanced MRI accurately identifies, quantifies, and maps tumor hypoxia in preclinical cancer models. *Cancer Res* 2016;76:787–95.
55. Rijpkema M, Kaanders JH, Joosten FB, van der Kogel AJ, Heerschap A. Effects of breathing a hyperoxic hypercapnic gas mixture on blood oxygenation and vascularity of head-and-neck tumors as measured by magnetic resonance imaging. *Int J Radiat Oncol Biol Phys* 2002;53:1185–91.